



# Low-temperature carbon monoxide and propane total oxidation by nanocrystalline cobalt oxides

G. Salek, P. Alphonse, P. Dufour, S. Guillemet-Fritsch, C. Tenailleau\*

Centre Interuniversitaire de Recherche et d'Ingénierie des MATériaux (CIRIMAT), UMR CNRS 5085, Université de Toulouse – UPS, 118 route de Narbonne, 31062 Toulouse cedex 09, France

## ARTICLE INFO

### Article history:

Received 29 June 2013

Received in revised form 1 August 2013

Accepted 7 August 2013

Available online 21 August 2013

### Keywords:

Cobalt oxides

Precipitation method

Catalysis

Carbon monoxide CO oxidation

Propane C<sub>3</sub>H<sub>8</sub> oxidation

## ABSTRACT

Pure CoO(OH), with intra particulate porosity up to 76%, was synthesized by an innovative aqueous precipitation method, starting either from nitrate or sulfate salts. Microstructural and chemical properties were characterized by powder X-ray diffraction (XRD), thermogravimetry (TG) and differential scanning calorimetry (DSC), scanning electron microscopy (SEM) and high-resolution transmission electron microscopy (HRTEM). The primary particles (10–15 nm) are self-organized in monolayer building hexagonal nano-platelets (50–200 nm) which are arranged randomly creating large pores.

CoO(OH) was converted in Co<sub>3</sub>O<sub>4</sub> by heating in air at 250 °C. This treatment did not modify the porosity but increased the specific surface area, which became close to 100 m<sup>2</sup>/g. The catalytic activity for CO and C<sub>3</sub>H<sub>8</sub> total oxidation was better for Co<sub>3</sub>O<sub>4</sub> than for CoO(OH). Besides, at high conversion rate, catalysts prepared from sulfate precursor showed a superior activity for C<sub>3</sub>H<sub>8</sub> oxidation than those prepared from nitrate. This effect can be explained by the improved accessibility of reactants to the surface of the catalysts which exhibit a larger porosity. To our knowledge, the activity values presented here are the highest reported in literature for C<sub>3</sub>H<sub>8</sub> total oxidation.

© 2013 Elsevier B.V. All rights reserved.

## 1. Introduction

Precious metal catalysts (Pt, Pd, Rh) have been commonly used in automotive and industrial catalytic converters since the 1980s for the total oxidation of CO and other exhaust gases [1,2]. Despite their high efficiency, their excessive cost and limited availability drives research scientists to explore alternative catalysts. Many investigations have demonstrated that single and mixed transition metal oxides could have an excellent catalytic activity on total oxidation of CO and hydrocarbons [3–6]. Among these oxides, Co<sub>3</sub>O<sub>4</sub> has been reported to be the best catalyst for oxidation of CO [5–11] and total oxidation of hydrocarbons [12–14]. However, Co<sub>3</sub>O<sub>4</sub> is not suitable for high temperature applications such as automotive converters because it loses oxygen above 900 °C [15] to form less active CoO or inactive CoAl<sub>2</sub>O<sub>4</sub> spinel when it is supported on alumina [16]. Nevertheless, it still remains a perfect candidate for low temperature applications like VOC removal.

Synthesis of Co<sub>3</sub>O<sub>4</sub> has been widely studied either by dry or wet methods. The wet methods used for preparing cobalt oxide include combustion [17], sol–gel [18], precipitation and coprecipitation [19–22], hydrothermal [23–25] and solvothermal [26].

Recently we reported a new synthesis process of Co–Mn spinel oxides [27] based on the precipitation at room temperature of nanocrystalline particles with a narrow size distribution, without using any polymeric agent. This low cost innovative process does not require any organic reactant and can be easily extended to large-scale production.

We used this new process for the synthesis of nanocrystalline CoO(OH). This oxyhydroxide was converted in Co<sub>3</sub>O<sub>4</sub> by heating in air. We present here the detailed materials characterizations and the study of their catalytic activity, for CO and C<sub>3</sub>H<sub>8</sub> total oxidations.

## 2. Experimental

### 2.1. Materials synthesis

Cobalt oxyhydroxide CoO(OH) was prepared by following our method described in a previous paper [27]. Co<sub>3</sub>O<sub>4</sub> was obtained after calcination of CoO(OH) in air.

Briefly, a solution of metallic salts was prepared by dissolving cobalt sulfate or cobalt nitrate (0.03 mol, 100 mL) in distilled water. Then, this solution was rapidly poured (5.5 L/s) into a LiOH solution (0.1 mol, 1400 mL) where the pH was kept at a constant value (12 ± 0.1) to obtain a homogenous precipitate. The precipitate was left under constant stirring for 30 min. The color then gradually changed from blue to brown which characterized the formation of

\* Corresponding author. Tel.: +33 0561556283.

E-mail address: [tenailleau@chimie.ups-tlse.fr](mailto:tenailleau@chimie.ups-tlse.fr) (C. Tenailleau).



$\text{Co}(\text{OH})_2$ . The precipitate was washed until the conductivity of wash water was less than  $10 \mu\text{S}/\text{cm}$ . Then, the wet hydroxide was dried at room temperature and  $\text{CoOOH}$  was formed. In the following, the ND and SD abbreviations will refer to the dry samples prepared from the nitrate and sulfate precursors, respectively.

## 2.2. Catalysts characterization

Residual lithium and sulfur contents were determined in the samples by Inductively Coupled Plasma Atomic Emission Spectroscopy (ICP-AES) using a Jobin Yvon (JY 2000) analyzer. X-ray Diffraction (XRD) measurements at room temperature were recorded on a Bruker D4-ENDEAVOR diffractometer, in the Bragg–Brentano geometry, using the  $\text{Cu K}\alpha$  radiation ( $40 \text{ kV}$ ,  $40 \text{ mA}$ ). Diffraction intensities were measured by scanning from  $10$  to  $100^\circ$  ( $2\theta$ ) with a step size of  $0.02^\circ$  ( $2\theta$ ). A quantitative estimation of the cell parameters and peak broadening was performed by profile fitting of the whole XRD patterns using the Fityk software [28]. An example of fitting is given in online resource 1. Peak profiles were modeled by a pseudo-Voigt function. Refined parameters included the zero shift ( $2\theta$ ), background, unit cell parameters and peak shapes. The refined FWHM (full-width at half-maximum) of the lines was used to compute, by the Scherrer's equation, the average crystallite size. The instrumental broadening contribution was evaluated by using a standard sample of  $\alpha$ -alumina.

To study the crystallographic phase transformation with temperature an Anton Paar HTK1200 N high-temperature chamber fitted on a Bruker D8-Advance diffractometer in the Bragg–Brentano geometry was used. The temperature was increased by steps of  $25^\circ\text{C}$  (heating rate of  $0.5^\circ\text{C}/\text{min}$ ) in the range  $100$ – $400^\circ\text{C}$ . The temperature was kept constant during each pattern acquisition.

Scanning electron microscopy (SEM) images were performed, on a JEOL JSM-6700F instrument while high resolution transmission electron microscopy (HR-TEM) observations were done on a JEOL 2100F instrument at  $200 \text{ kV}$ , both equipped with a Field Emission Gun (FEG). Samples were prepared by putting a drop of an ethanol suspension of particles either on a glass substrate (SEM) or on a carbon-coated Cu grid (TEM).

Thermogravimetric/differential scanning calorimetry (TGA/DSC) analyses were carried out on a Mettler-Toledo TGA-DSC1 device using aluminum crucibles. Experiments were performed with  $20\%$   $\text{O}_2$  in Ar dynamic atmosphere (flow rate of  $50 \text{ cm}^3/\text{min}$ ) using a heating ramp of  $5^\circ\text{C}/\text{min}$  from room temperature to  $600^\circ\text{C}$ .

Specific surface area and pore size distribution were calculated from nitrogen adsorption–desorption isotherms collected at  $77 \text{ K}$ , using an adsorption analyzer Micromeritics Tristar II 3020. The specific surface areas were computed from adsorption isotherms, using the Brunauer–Emmett–Teller (BET) method [29]. The pore size distributions (PSD) were computed from desorption isotherms by the Non Local Density Functional Theory (NLDFT) method [30] (with Quantachrome Autosorb-1 software). Pore volume ( $P_v$ ) was calculated from the adsorbed volume ( $V_a$ ) at a relative pressure of  $0.995$  by:

$$P_v = V_a \times \left( \frac{\text{N}_2 \text{ gas density}}{\text{N}_2 \text{ liquid density}} \right) = 0.00155 V_a$$

Each sample was degassed at  $150^\circ\text{C}$  overnight ( $\sim 16 \text{ h}$ ) prior to analysis in order to remove the species adsorbed on the surface.

## 2.3. Determination of catalytic activity

These tests were performed in a differential, tubular, fixed bed flow reactor, at ambient pressure, with a residence time  $\approx 0.03 \text{ s}$  (catalyst mass =  $0.050 \text{ g}$ , volumetric flow rate =  $1.63 \text{ cm}^3 \text{ s}^{-1}$ ). Reactants were dosed by mass flow controllers (Brooks 5850). The

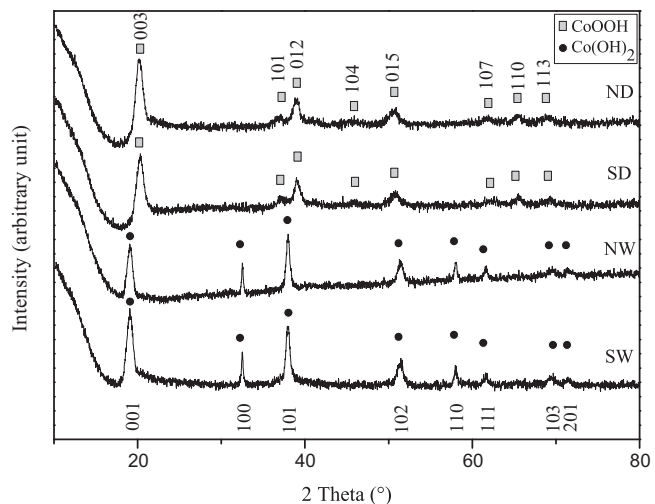


**Fig. 1.** XRD patterns of SD and ND samples. Bragg peak indices are indicated for each structure: trigonal with the  $P3m1$  space group for  $\text{Co}(\text{OH})_2$  and trigonal with the  $R-3m$  space group for  $\text{CoO}(\text{OH})$ .

catalyst temperature was controlled by a K-type thermocouple positioned inside the catalyst bed. For CO oxidation the temperature range was  $30$ – $200^\circ\text{C}$  and the inlet gas composition was  $0.8\%$   $\text{CO}$  +  $20\%$   $\text{O}_2$  in Ar. For  $\text{C}_3\text{H}_8$  oxidation the temperature range was  $30$ – $300^\circ\text{C}$  and the inlet gas composition was  $0.4\%$   $\text{C}_3\text{H}_8$  +  $20\%$   $\text{O}_2$  in Ar. The catalyst temperature was increased at a heating rate of  $150^\circ\text{C}/\text{h}$  during the CO oxidation and  $200^\circ\text{C}/\text{h}$  during the propane oxidation.

The gas phase composition during the tests was monitored by mass spectrometry (HPR20-QIC from Hiden Analytical). Unless otherwise specified, the catalysts were first pretreated with  $20\%$   $\text{O}_2$  in Ar for  $60 \text{ min}$ . To study the catalytic activity of  $\text{CoO}(\text{OH})$  the thermal treatment temperature was either  $140$  or  $180^\circ\text{C}$ ; for  $\text{Co}_3\text{O}_4$  the temperature was either  $250$  or  $300^\circ\text{C}$ .

## 3. Results and discussion

### 3.1. Elemental analysis

The lithium residual content in our materials, determined by ICP, was  $32 \pm 2 \text{ ppm}$  for SD and  $33 \pm 2 \text{ ppm}$  for ND. These values are considered to be insignificant to have a measurable effect on the microstructure or catalytic activity.

### 3.2. X-ray diffraction study

**Fig. 1** shows the room temperature XRD patterns of wet sample SW (sulfate precursor), NW (nitrate precursor) and SD and ND samples. Wet samples patterns show only the lines of cobalt  $\beta$ -hydroxide  $\text{Co}(\text{OH})_2$  which has a trigonal structure (hexagonal lattice) with the  $P-3m1$  space group (no. 164). Cell parameters and FWHM were obtained from profile fitting of the whole XRD patterns. The data are reported in **Table 1**. Cell parameters are close to those reported in literature ( $a = 0.317$  and  $c = 0.464 \text{ nm}$  [JCPDS card 01-074-1057]). A significant difference between the  $001$  and  $100$  peak widths are observed, which indicates an anisotropy in the crystallites shapes.

XRD patterns of dried samples show that only the oxyhydroxide  $\text{CoO}(\text{OH})$  phase is formed. This compound crystallizes with a trigonal symmetry (hexagonal lattice) and the  $R-3m$  space group (no. 166). Cell parameters and FWHM obtained from profile fitting are also reported in **Table 1**. The  $a$  cell parameter, determined after refinement, is close to the value reported in literature whereas  $c$  is

**Table 1**

Cell parameters and size of diffraction domains calculated from FWHM for the main lines for wet and dried samples.

Reference	Formula	<i>a</i> (nm)	<i>c</i> (nm)	D_001 (nm)	D_100 (nm)	D_101 (nm)
NW	Co(OH) <sub>2</sub>	0.318	0.466	9.5	40.2	16.2
SW	Co(OH) <sub>2</sub>	0.318	0.465	9.3	45.6	17.4
Reference	Formula	<i>a</i> (nm)	<i>c</i> (nm)	D_003 (nm)	D_012 (nm)	D_015 (nm)
ND	CoO(OH)	0.286	1.324	7.6	6.4	5.8
SD	CoO(OH)	0.286	1.326	9.4	9.0	7.3

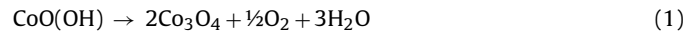
significantly larger (*a* = 0.285 nm, *c* = 1.315 nm, JCPDS card 01-073-1213). Compared to hydroxide, the CoO(OH) crystallites seem less anisotropic.

The structural phase transformation induced by heating CoO(OH) in air was followed by HT-XRD. A series of XRD patterns recorded, every 25 °C, for sample SD are plotted in Fig. 2. The strongest 003 line of CoO(OH) vanishes between 200 and 225 °C, while the 220 line of Co<sub>3</sub>O<sub>4</sub> is observed from 200 °C. The phase transformation CoO(OH) → Co<sub>3</sub>O<sub>4</sub> was fully completed at 225 °C in air. A similar trend is observed in the case of the ND samples (see online resource 2).

### 3.3. TG-DTG analysis

The thermogravimetric (TG), its derivative (DTG) and the heat flow (Hf) curves of the SD and ND samples are plotted in Fig. 3. While the sample mass continuously decreases as the temperature increases, the TG and DTG plots of the SD sample shows three main changes (top graph). A first small variation around 100 °C, can be attributed to the loss of water adsorbed at the surface of the particles. At the end of this stage the total mass loss is 1.4%. During the second stage, in the range 120–226 °C, a small DTG peak and a broad exothermic Hf peak is observed. The heat produced at this stage, calculated by integrating the Hf curve between 120 and 226 °C, is 218 J/g. The associated mass loss represents 2.6%. No structural transformation was evidenced by HT-XRD analysis in this temperature range (see Fig. 2). Note that this peak is hardly visible on the Hf curve of ND sample because its intensity is about 10 times lower (Fig. 3, bottom graph). One possible explanation could be that oxyhydroxide contained residual Co<sup>2+</sup> which are oxidized at this temperature. The third step, above 226 °C, shows the largest mass loss and is associated with a large DTG peak (*T*<sub>min</sub> = 286 °C) and an endothermic peak on the Hf curve (*T*<sub>min</sub> = 286 °C). The heat related to this step, calculated by integration of DSC curve is 158 J/g. Since the HT-XRD measurements showed that the transformation

of CoO(OH) in Co<sub>3</sub>O<sub>4</sub> starts at 200 °C (see Fig. 2), this final step corresponds to the formation of Co<sub>3</sub>O<sub>4</sub> according to the following reaction:



The expected mass loss for this reaction is 12.7%. Actually at the end of the DTG peak (295 °C), the sample mass is still larger than expected for Co<sub>3</sub>O<sub>4</sub> formation and the TG curve slowly decreases up to 600 °C. This can be explained by assuming that the oxide formed at 295 °C is non-stoichiometric due to an excess of Co<sup>3+</sup> cations. These Co<sup>3+</sup> will slowly reduce into Co<sup>2+</sup> at higher temperature explaining the negative drift of the Hf curve observed in the 300–600 °C temperature range.

TG curves of the ND and SD samples are very similar but Hf curves differ mainly at the second step with a much lower exothermic release. The heat produced at this stage (20 J/g, calculated by the integration of the Hf curve) is more than ten times lower than the heat measured for the SD sample. This would indicate that ND sample is almost stoichiometric probably because, unlike the sulfate, the nitrate anion is an oxidizer.

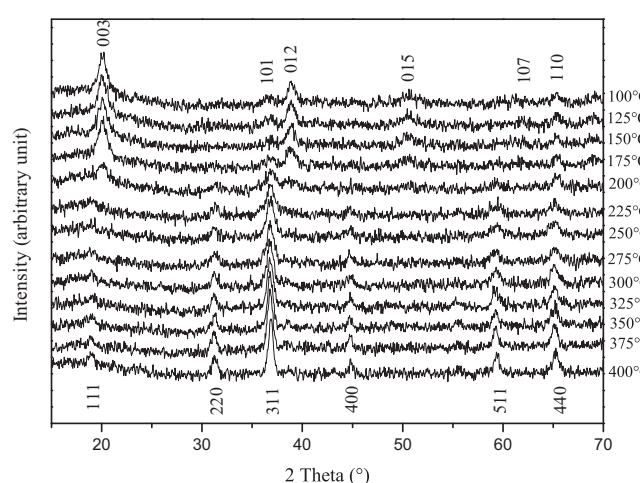


Fig. 2. HT-XRD patterns of SD sample.

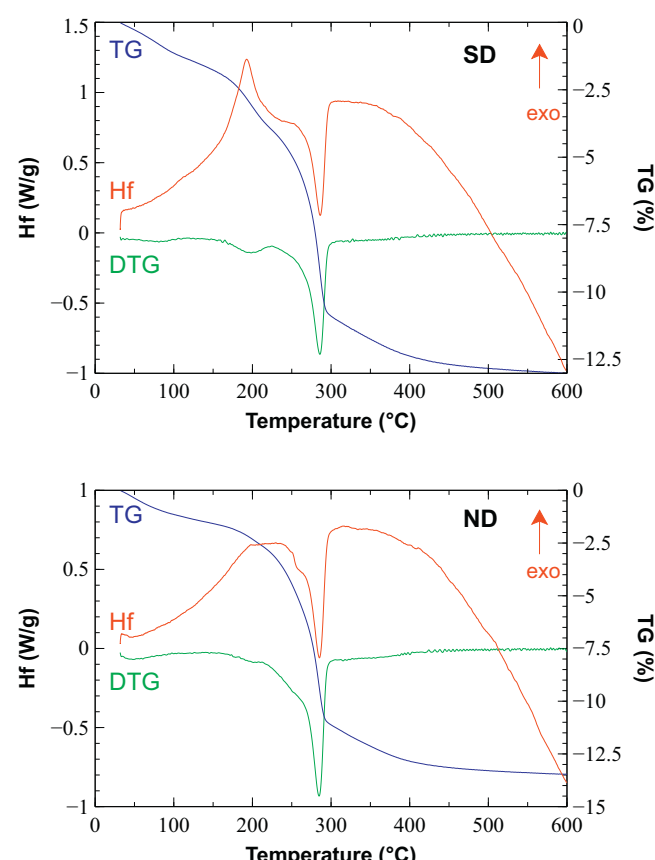
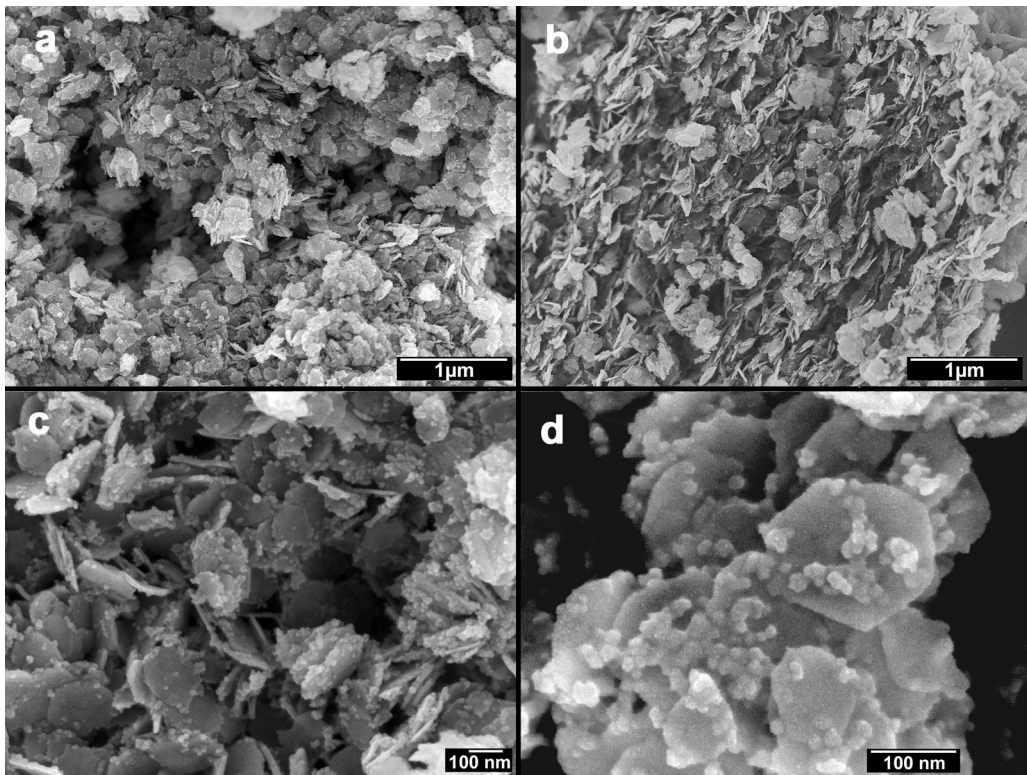


Fig. 3. TG-DSC analysis of CoO(OH) samples prepared from sulfate precursor (SD) and nitrate precursor (ND).



**Fig. 4.** SEM images of the (a, c, d) SD and (b) ND samples.

### 3.4. Microstructural characterizations

SEM images of  $\text{CoO(OH)}$  synthesized from sulfate (a) and nitrate (b) precursors are presented in Fig. 4a and b, respectively. Nano-platelets aggregate to create a very porous network. The shape and size of these particles are similar regardless the precursor used. This could be explained by the dilute medium used during the synthesis process which would minimize the influence of the anions. The morphology of these materials are rather similar to the  $\text{CoO(OH)}$  nano-discs, also prepared by precipitation, by Yang et al. [22].

Higher magnification SEM images (see Fig. 4c and d) reveal that the platelet shape is hexagonal, following their

crystallographic structure. The platelets width varies from 50 to 200 nm and their thickness from 10 to 15 nm. A large amount of nanoparticles (15–20 nm in diameter) are attached to the surface of each plate. Sometimes it can be seen that these particles are not spherical but close to the hexagonal shape like that observed for most of the large plates (see Fig. 4d). These small particles prevent close packing of the platelets, and strongly contribute to the porosity of aggregates.

HR-TEM images show that smaller particles are single crystals and hexagonal platelets do not seem to result from the agglomeration of these small crystallites (Fig. 5).

SEM or TEM images before and after calcination at 300 °C show no modifications of the microstructure of these materials. This is in

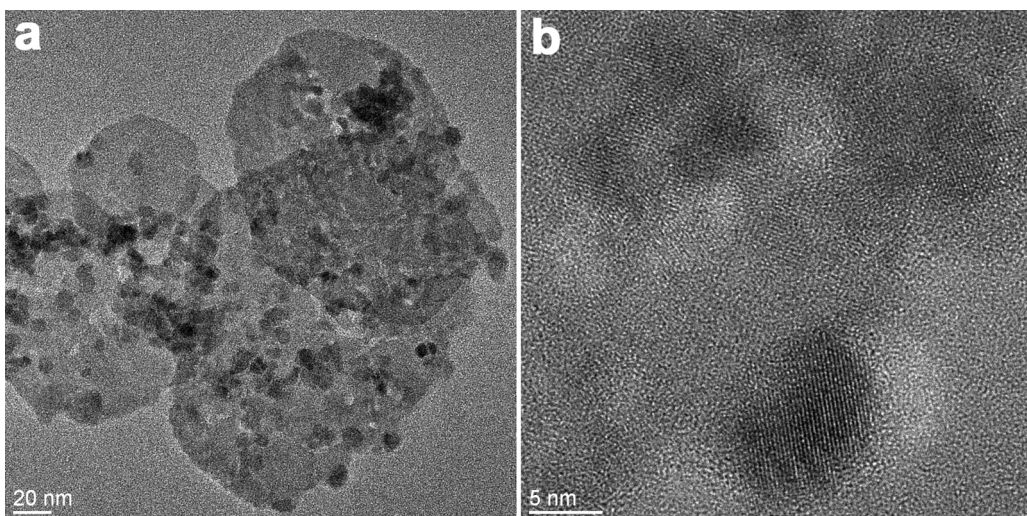


**Fig. 5.** TEM images of (a) SD and (b) ND  $\text{CoO(OH)}$  samples.

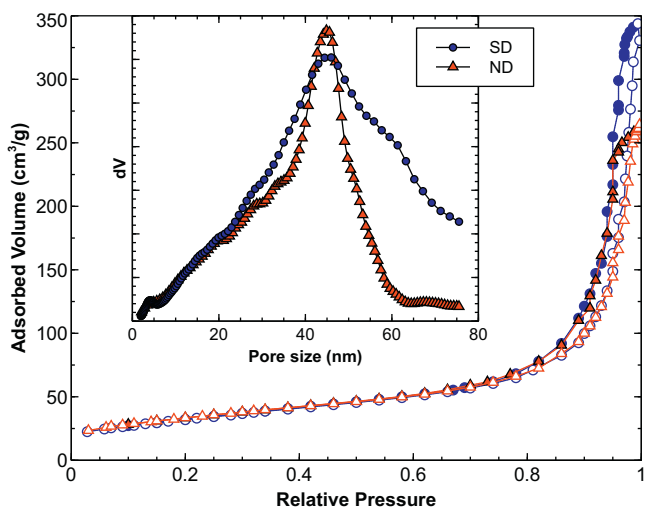


**Fig. 6.**  $\text{N}_2$  adsorption–desorption isotherms and pore size distributions (PSD) for catalysts heated at 250 °C. Open symbols correspond to adsorption and full symbols to desorption.

agreement with previous research works showing that the conversion of these  $\text{CoO(OH)}$  nano-objects into  $\text{Co}_3\text{O}_4$  is topotactic [22].

### 3.5. Surface and porosity by $\text{N}_2$ adsorption

The nitrogen adsorption–desorption isotherms of the  $\text{CoO(OH)}$  samples are plotted in Fig. 6. Despite their H1-type hysteresis loop, these isotherms are close to the type II [31]. They reveal that nitrogen was mainly adsorbed at relative pressures higher than 0.9, demonstrating that most of the pores have a size exceeding 20 nm. The BET surface area  $S_{\text{BET}}$  and pore volume  $V_{\text{pore}}$  of the samples are reported in Table 2. The oxyhydroxide prepared from the sulfate precursor has a lower surface area but a larger pore volume.

The pore size distributions (PSD), calculated from the NLDFT method [30], are very broad (see inset in Fig. 6). For  $\text{CoO(OH)}$  prepared from nitrate precursor (ND) most of the pores are large mesopores ( $<50$  nm) whereas about 40% of the pores are macropores for those prepared with sulfate precursor (SD). These PSD are in agreement with the particle aggregates observed by SEM. The small mesopores ( $<10$  nm) correspond to the voids between the stacking plates whereas the largest pores result from the voids between the set of stacking plates. It should be emphasized here that this kind of structure produces unsupported catalysts with outstanding porosity. For example, in the case of SD calcined at 250 °C, a pore volume of 0.53 cm<sup>3</sup>/g with a density of 6.11 g/cm<sup>3</sup> corresponds to a porosity of 76% (see Table 2).

$\text{CoO(OH)}$  samples treated at 250 °C transformed in  $\text{Co}_3\text{O}_4$ . For both precursors, this phase transformation was accompanied by a

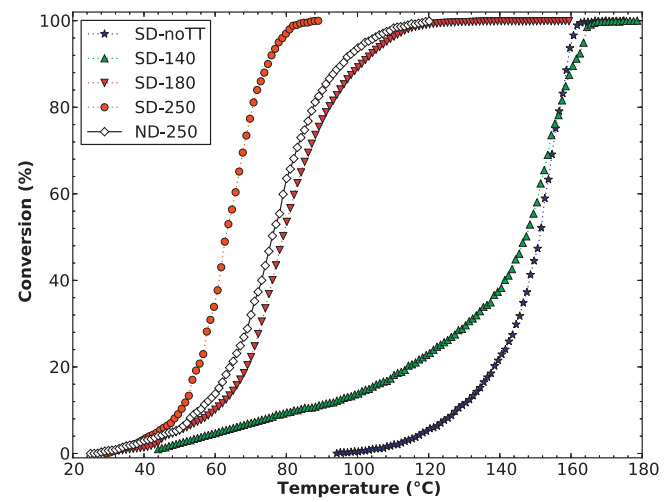


**Fig. 7.** Variation of the CO conversion with the reaction temperature.

$S_{\text{BET}}$  enlargement of about 40% but the pore volume did not change. According to Eq. (1) this conversion corresponds to a mass loss of 12.7%. Hence, if this reaction occurs without any modification of the surface area, the specific surface area is expected to increase only by 14.5%.

$S_{\text{BET}}$  of the oxides dropped down to values close to those of  $\text{CoO(OH)}$  after calcination at 300 °C. Again the pore volume was not modified by this transformation.

### 3.6. Catalytic tests

#### 3.6.1. Activity for total oxidation of CO

Carbon monoxide conversion vs. temperature plots, recorded on SD samples, are shown in Fig. 7. Without preliminary thermal treatment of the catalyst the conversion did not start below 100 °C (SD-noTT). This was due to the adsorbed water, which is known to inhibit the activity for the CO oxidation [8,16]. The second test, performed on the same catalyst (SD-180), which did not show this inhibition period confirmed this hypothesis. For this test 100% conversion was achieved at 100 °C. XRD measurements of the catalyst after test showed that the  $\text{CoO(OH)}$  phase remained and no structural transformation occurred as it can be expected when the temperature does not exceed 180 °C. For the sample referred as SD-140, the thermal treatment temperature at 140 °C was not high enough to obtain a full activity.

For the sample referred to as SD-250, which had the best catalytic activity, XRD analysis performed after the test revealed that the catalyst was transformed into  $\text{Co}_3\text{O}_4$ . The strong activity measured for SD-250 can be explained by the highest catalytic activity observed for  $\text{Co}_3\text{O}_4$  compared to that of  $\text{CoO(OH)}$  for the CO oxidation [9]. However, we have seen in Table 2 that this conversion produced also a 40% expansion of the specific surface area, which its effect cannot be ruled out.

For low conversions, below 3%, the activities of ND samples were similar to the activities of SD samples pre-treated at the same temperatures. However, when conversion exceeded 3%, ND activity became lower. For example, Fig. 7 shows a plot of a ND catalyst which has undergone a thermal treatment at 250 °C (ND-250). XRD patterns did not show any significant difference between these  $\text{Co}_3\text{O}_4$  oxides. Though the specific surface area of ND was slightly higher than SD, the pore volume of SD was 25% larger (see Table 2). As the CO oxidation is a very fast reaction, the better accessibility of CO to the SD surface could explain its superior activity at high conversion rate.

**Table 2**

Effect of thermal treatment temperature of catalysts on their BET specific surface area ( $S_{\text{BET}}$ ) and pore volume ( $P_v$ ). Density was calculated from cell parameters given in Table 1. Porosity was calculated using the classical formula: Porosity =  $P_v/(P_v + 1/\text{density})$ .

Reference	Structure	Calculated density (g/cm <sup>3</sup> )	$S_{\text{BET}}$ (m <sup>2</sup> /g)	$P_v$ (cm <sup>3</sup> /g)	Porosity (%)
SD-150	$\text{CoO(OH)}$	4.95	$81 \pm 5$	$0.52 \pm 0.04$	72
ND-150	$\text{CoO(OH)}$	4.95	$88 \pm 5$	$0.42 \pm 0.03$	76
SD-250	$\text{Co}_3\text{O}_4$	6.11	$114 \pm 6$	$0.53 \pm 0.04$	76
ND-250	$\text{Co}_3\text{O}_4$	6.11	$119 \pm 6$	$0.41 \pm 0.03$	68
SD-300	$\text{Co}_3\text{O}_4$	6.11	$84 \pm 5$	$0.51 \pm 0.04$	71
ND-300	$\text{Co}_3\text{O}_4$	6.11	$90 \pm 5$	$0.42 \pm 0.03$	72

**Table 3**

Comparison of catalyst activity for propane oxidation at 200 °C.

Reference	Catalyst mass (g)	Inlet flow (cm <sup>3</sup> /min)	Inlet concentration (%)	Conversion at 200 °C (%)	Activity at 200 °C (μmol s <sup>-1</sup> g <sup>-1</sup> )
Ref. [32]	0.25	50	0.80	0.41	0.45
Ref. [33]	0.25	50	0.80	0.52	0.57
SD-250	0.05	98	0.37	0.34	1.69
SD-300	0.05	98	0.37	0.13	0.64
ND-250	0.05	98	0.37	0.14	0.71

Many authors have reported catalyst deactivation for CO oxidation near room temperature [6]. Though formation of stable surface carbonates species are observed, they are not the cause of the deactivation. Jansson et al. [11] suggested that the explanation is the surface reconstruction with the transformation of active octahedral  $\text{Co}^{3+}$  sites into inactive tetrahedral  $\text{Co}^{3+}$ . We have tested the stability of CO conversion on SD-250 working at 70 °C. After 3 h on stream the conversion changed very little, from 77% to 76% (see online resource 3).

### 3.6.2. Activity for total oxidation of propane

Propane conversion against temperature, recorded on SD samples, is shown in Fig. 8. This reaction occurs at a higher temperature than for CO oxidation.

Unlike what was observed in CO oxidation, the catalytic activity was not significantly modified when the catalyst was not pre-treated in 20%  $\text{O}_2$  before the propane oxidation test. Besides, the thermal treatment temperature should not exceed 250 °C. For example, after a thermal treatment at 300 °C, the propane conversion at 200 °C dropped from 34% down to 13%. The change in surface area induced by the thermal treatment at 300 °C (≈25%) does not seem to be large enough to explain such a drop. We believe that it could be related to a more stoichiometric phase.

At the beginning of the catalytic test, the sample pre-treated at 180 °C (SD-180) was the oxyhydroxide  $\text{CoO(OH)}$ . As for CO oxidation, its activity was lower than for  $\text{Co}_3\text{O}_4$ . However, during the test it was converted in  $\text{Co}_3\text{O}_4$  so that, at the end of the experiment, its activity became the same as that of SD-250. As for CO oxidation, for high conversions, above 6%, the activities of ND samples were always lower than the activities of SD samples. An example is given for the ND catalyst pre-treated at 250 °C (ND-250) in Fig. 8. ICP analysis performed on samples prepared from sulfate showed the presence of sulfur ( $0.25 \pm 0.05$  wt%). Thus it is possible that the associated sulfate groups could increase the surface acidity and

promote the propane oxidation explaining the better activity of catalysts prepared from sulfate precursor.

To compare the catalytic activity of our materials with the data reported in the literature we calculated the specific activity defined by the number of  $\mu\text{mol}$  of reactant ( $\text{C}_3\text{H}_8$ ) converted per second and per g of catalyst. As it was demonstrated that CO conversion is strongly dependent upon the amount of water in the reactants [4,8,16] we limited our comparison to propane oxidation. The activities reported in Table 3 show that the most active catalysts are those prepared by our method, despite the fact that the catalysts reported elsewhere have a larger specific surface area (100 m<sup>2</sup>/g for [31] and 122 m<sup>2</sup>/g for [32]). Garcia et al. [33] prepared their catalysts by a nanocasting route using mesoporous silica as a hard template. It is worth noticing that their most active catalyst was not the one developing the largest specific surface area (173 m<sup>2</sup>/g) but the one having the largest pore size and pore volume. This result supports our previous hypothesis on the key role of the pore size and pore volume on the activity at high conversion.

## 4. Conclusions

$\text{CoO(OH)}$ , with a porosity up to 76%, was synthesized by an easy and inexpensive precipitation process without using any structure directing agent or pore former. This cobalt oxyhydroxide was converted in  $\text{Co}_3\text{O}_4$  by calcination at 250 °C. The phase transformation did not modify the porosity but increased the specific surface area, which became close to 100 m<sup>2</sup>/g. The outstanding porosity of these cobalt oxides results both from their crystallization in hexagonal nano-platelets and from the random arrangement of these nano-objects creating large pores.

The catalytic activity for CO and  $\text{C}_3\text{H}_8$  total oxidation was superior for  $\text{Co}_3\text{O}_4$  than for  $\text{CoO(OH)}$ . Besides, catalysts prepared from sulfate precursor showed a higher activity at high conversion rate than prepared from nitrate. Since the only difference found between them was their textural characteristics, we believe that the higher activity could be explained by the improved accessibility of reactants to the surface of the catalysts that have the higher porosity. Our catalysts showed a superior activity for  $\text{C}_3\text{H}_8$  total oxidation than any other catalysts reported in the literature.

## Appendix A. Supplementary data

Supplementary data associated with this article can be found, in the online version, at <http://dx.doi.org/10.1016/j.apcatb.2013.08.015>.

## References

- [1] Y.-F. Yu Yao, J. Catal. 87 (1984) 152–162.
- [2] R.M. Heck, R.J. Farrauto, Catalytic Air Pollution Control, 2nd ed., Wiley, New York, 2002, pp. 69–129 (Chapter 6).
- [3] J.W. Saalfrank, W.F. Maier, Angew. Chem. 116 (2004) 2062–2066.
- [4] X. Xie, Y. Li, Z.-Q. Liu, M. Haruta, W. Shen, Nature 458 (2009) 746–749.
- [5] S. Royer, D. Duprez, Catal. ChemCatChem 3 (2011) 24–65.
- [6] C.B. Wang, C.W. Tang, H.C. Tsai, S.H. Chien, Catalysis Letters 107 (2006) 223–230.
- [7] D. Berger, F. Morfin, C. Matei, J.C. Volta, J. Optoelectron. Adv. Mater. 9 (2007) 1540–1545.
- [8] F. Grillo, M.M. Natile, A. Glisenti, Appl. Catal. B: Environ. 48 (2004) 267–274.

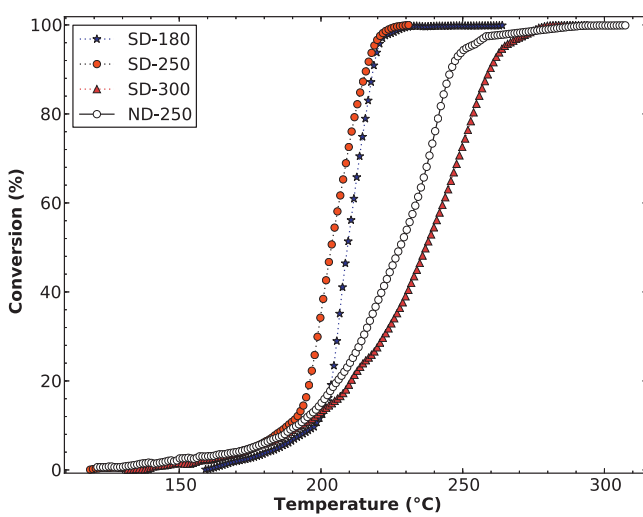


Fig. 8. Variation of the propane conversion with the reaction temperature.

- [9] H.-K. Lin, C.-B. Wang, H.-C. Chiu, S.-H. Chien, *Catal. Lett.* 86 (2003).
- [10] Y.J. Mergler, J. Hoebink, B.E. Nieuwenhuys, *J. Catal.* 167 (1997) 305–313.
- [11] J. Jansson, M. Skoglundh, E. Fridell, P. Thormählen, *Top. Catal.* 16–17 (2001) 385–389.
- [12] T.E. Davies, T. García, B. Solsona, S.H. Taylor, *Chem. Commun.* 32 (2006) 3417–3419.
- [13] J.G. McCarthy, Y.F. Chang, V.L. Wong, M.E. Johansson, *Prep. Am. Chem. Soc. Div. Petrol. Chem.* 42 (1997) 158–164.
- [14] L.F. Liotta, G. Di Carlo, G. Pantaleo, A.M. Venezia, G. Deganello, *Appl. Catal. B: Environ.* 66 (2006) 217–227.
- [15] R. Jin, Y. Chen, W. Li, Wei Cui, Y. Ji, C. Yu, Yi Jiang, *Appl. Catal. A: Gen.* 201 (2000) 71–80.
- [16] Y. Fang Yu Yao, *J. Catal.* 33 (1974) 108–122.
- [17] M. Salavati-Niasari, N. Mir, F. Davar, *J. Phys. Chem. Solids* 70 (2009) 847–852.
- [18] F. Svegl, B. Orel, I. Grabec-Svegl, V. Kaucic, *Electrochim. Acta* 45 (2000) 4359–4371.
- [19] I. Lopez, T. Valdes-Solis, G. Marban, *ChemCatChem* 3 (2011) 734–740.
- [20] J.-W. Wang, Y.-M. Kuo, *J. Nanomater.* 2013 (2013).
- [21] S. Zhuiykov, *Materials Forum* 31 Australia, 2007.
- [22] J. Yang, H. Liu, W.E.N. Martens, R.L. Frost, *J. Phys. Chem. C* 114 (2010) 111–119.
- [23] Y. Zhang, Y. Chen, T. Wang, J. Zhou, Y. Zhao, *Microporous Mesoporous Mater.* 114 (2008) 257–261.
- [24] Y. Chen, Y. Zhang, S. Fu, *Mater. Lett.* 61 (2007) 701–705.
- [25] S.K. Tripathy, M. Christy, N.-H. Park, E.K. Suh, S. Anand, Y.T. Yu, *Mater. Lett.* 62 (2008) 1006–1009.
- [26] X. Jing, S. Song, J. Wang, L. Ge, S. Jamil, Q. Liu, T. Mann, Y. He, M. Zhang, H. Wei, L. Liu, *Powder Technol.* 217 (2012) 624–628.
- [27] G. Salek, S. Guillemet-Fritsch, P. Dufour, C. Tenailleau, *Int. J. Chem.* 4 (2012) 44–53.
- [28] M. Wojdyl, *J. Appl. Crystallogr.* 43 (2010) 1126–1128.
- [29] S. Brunauer, P. Hemmett, E. Teller, *J. Am. Chem. Soc.* 60 (1938) 309–319.
- [30] N. Seaton, J. Walton, N. Quirke, *Carbon* 27 (1989) 853–861.
- [31] K.S.W. Sing, D.H. Everett, R.A.W. Haul, L. Moscou, R.A. Pierotti, J. Rouquerol, T. Siemieniewska, *Pure Appl. Chem.* 57 (1985) 603–619.
- [32] B. Solsona, T.E. Davies, T. García, I. Vazquez, A. Dejoz, S.H. Taylor, *Appl. Catal. B: Environ.* 84 (2008) 176–184.
- [33] T. García, S. Agouram, J.F. Sanchez-Royo, R. Murillo, A.M. Mastral, A. Aranda, I. Vazquez, A. Dejoz, B. Solsona, *Appl. Catal. A: Gen.* 386 (2010) 16–27.